I&EC research
Industrial & Engineering Chemistry Research

Article

Cite This: Ind. Eng. Chem. Res. 2018, 57, 4277−4286

pubs.acs.org/IECR

Cellulose Microfiber-Supported TiO_2@Ag Nanocomposites: A Dual-Functional Platform for Photocatalysis and *in Situ* Reaction Monitoring

Guolin Zhang,[†] Long Chen,[†] Xiaoqi Fu,*[,†] and Hui Wang*[,‡]

[†]School of Chemistry and Chemical Engineering, Jiangsu University, Zhenjiang, Jiangsu 212013, China

[‡]Department of Chemistry and Biochemistry, University of South Carolina, Columbia, South Carolina 29208, United States

Supporting Information

ABSTRACT: Photocatalytic degradation of toxic organic pollutants in aquatic environments provides an efficient, cost-effective, and sustainable approach to environmental remediation. The optimization of photocatalytic detoxification processes essentially relies not only on the capability to fine-tailor the structures and compositions of the photocatalysts but also on detailed understanding of the mechanisms that dictate the photocatalytic interfacial molecular transformations. Here we have designed and constructed a hierarchically organized suprastructure comprising TiO_2@Ag nanocomposite particles supported by cellulose microfiber matrices, which serves as both an efficient photocatalyst for the photodegradation of 4-chlorophenol into mineralized small molecules and a robust substrate for plasmon-enhanced molecular spectroscopy. Such dual functionalities provide unique opportunities for us to precisely monitor, in real time, the detailed photocatalytic molecular transformations occurring at the molecule−catalyst interfaces using surface-enhanced Raman scattering as an ultrasensitive, time-resolving, and molecular fingerprinting spectroscopic tool.

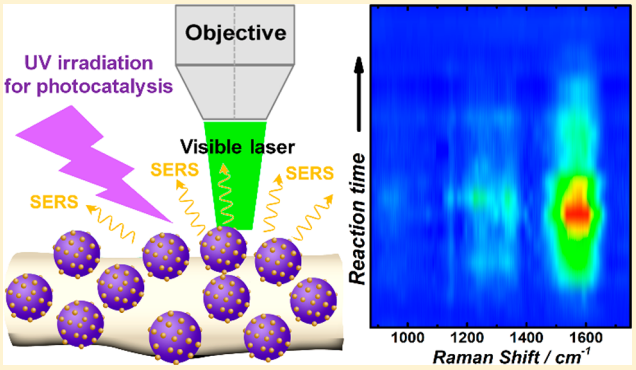

1. INTRODUCTION

The ever-incrementing industrial and agricultural activities generate increasing amounts of hazardous organic pollutants released into aquatic environments, causing serious environmental and health concerns worldwide. An effective and sustainable approach to environmental remediation has been photocatalytic degradation of toxic organic pollutants into mineralized small molecules, such as CO_2 and H_2O, under mild ambient conditions.[1−6] The rational optimization of these photocatalytic detoxification processes requires quantitative understanding of not only the structure−composition−property relationships of the photocatalysts but also the detailed mechanisms dictating the chemical transformations at the molecule−photocatalyst interfaces. As well-exemplified by the chlorophenol compounds,[7−11] organic pollutants may undergo mechanistically complex photocatalytic degradation processes involving multiple intermediates along distinct molecule-transforming pathways. Some intermediates derived from the photocatalytic reactions may be long-lived and even more toxic than their parental organic pollutants.[7−9] A variety of *ex situ* molecular characterization techniques, such as UV−vis absorption spectroscopy,[12] high performance liquid chromatography,[13] electrochemical analysis,[14] and gas chromatography/mass spectrometry,[15] have been used as analytical tools to resolve the apparent photocatalytic reaction kinetics and detect the kinetically trapped intermediates. However, these *ex situ* techniques lack the capabilities to precisely monitor the reactions in real time and simultaneously provide molecular fingerprinting information. Therefore, it has recently stimulated tremendous interests to develop dual-functional materials systems that integrate superior photocatalytic performances with unique capabilities to track detailed molecular transformations *in situ*.[16−20]

While the photocatalytic performance can be systematically optimized by fine-tailoring the compositions, structures, and surface dopants of the photocatalysts,[21−28] incorporation of sensitive *in situ* molecular sensing functionalities into photocatalytically active materials still remains a challenging task. Here we have designed and constructed a hierarchical suprastructure consisting of cellulose microfiber (CMF)-supported TiO_2@Ag nanocomposite particles, denoted as TiO_2@Ag/CMFs, which serves as a dual-functional platform for both high-performance heterogeneous photocatalysis and *in situ* reaction monitoring using surface-enhanced Raman scattering (SERS) as an ultrasensitive, time-resolving spectro-

Received: January 1, 2018
Revised: March 5, 2018
Accepted: March 9, 2018
Published: March 9, 2018

DOI: 10.1021/acs.iecr.8b00006
Ind. Eng. Chem. Res. 2018, 57, 4277−4286

scopic tool. Cellulose microfibers (CMFs) are a linear homopolymer ubiquitously existing in plants with highly abundant hydroxyl groups, forming a compact supramolecular semicrystalline structure.[29] Upon treatments with acids, the compact CMFs undergo a swelling process to form a three-dimensional (3D) network structure with superhydrophilic open surfaces,[30] providing an ideal support matrix for photocatalysts.[31,32] We demonstrate that photocatalytically active submicrometer TiO_2 particles with rough surfaces can be grown directly on the CMF supports through a straightforward hydrolysis process. TiO_2 has been a semiconductor material widely used for the photocatalytic degradation of organic pollutants in water primarily owing to its desired optical properties, low cost, excellent photostability, and versatility of surface functionalization.[1,4,22,33,34] We decorate the surfaces of CMF-supported TiO_2 particles with densely distributed Ag nanoparticles not only to further enhance the photocatalytic activity of TiO_2 under UV illumination but also to create intense plasmonic field enhancements exploitable for SERS-based structural characterizations of molecular adsorbates. SERS is an intriguing nonlinear optical phenomenon in which the Raman signals of molecules adsorbed on the surfaces of plasmonic nanostructures are enormously amplified by many orders of magnitude,[35−40] approaching even single-molecule detection sensitivity when the plasmonic field enhancements become sufficiently high.[41−44] Benefiting from its unique time-resolving and molecular fingerprinting capabilities combined with high detection sensitivity, SERS has become a powerful plasmon-enhanced spectroscopic tool for *in situ* monitoring of interfacial molecular transformations on plasmonic nanoparticle surfaces.[45−51]

Among a large library of organic pollutants, chlorophenols constitute a family of recalcitrant pollutants that are easily accumulated in aquatic environments and in the bodies of living creatures but highly resistant against mineralization under natural conditions.[52,53] Heterogeneous photocatalysis offers so far one of the most economic and effective ways to remove toxic chlorophenol compounds from contaminated water samples.[10,11,54] Therefore, we chose the photocatalytic degradation of 4-chlorophenol (4-CP) in aqueous solution at room temperature as a model reaction for detailed spectroscopic investigations using the as-constructed TiO_2@Ag/CMFs as both the photocatalysts and the SERS substrates. The capability to probe the temporal evolution of detailed molecular structures on photocatalyst surfaces in real time provides unique opportunities to unambiguously identify the reaction intermediates and fully understand the complex reaction mechanisms.

2. EXPERIMENTAL DETAILS

2.1. Chemicals and Materials. Silver nitrate ($AgNO_3$, 99.995%) and ammonium hexafluorotitanate ($(NH_4)_2{\cdot}TiF_6$, 99.99%) were purchased from Alfa Aesar. 4-CP, hydroquinone (HQ), 1,4-benzonquinone (BQ), boric acid (H_3BO_3, 99.95%), sulfuric acid (H_2SO_4, 98%), dimethyl sulfoxide (DMSO, 99.5%), and glucose ($C_6H_{12}O_6$, 99.5%) were purchased from Sinopharm Chemical Reagent Co., Ltd. (Shanghai, China). Quinhydrone (97%) was purchased from Sigma-Aldrich. Compressed cellulose fibers (0.10 cm thick) were purchased from Gold East Paper Co., Ltd. (Jiangsu, China). All reagents were used as received without further purification. Ultrapure water (18.2 MΩ resistivity) distilled through a Millipore water purification system was used for all experiments.

2.2. Synthesis of TiO_2@Ag/CMFs. A piece of 0.1 cm thick cellulose paper comprising compressed CMFs was cut into 1 cm × 1 cm pieces, immersed in DMSO at 80 °C for 3 h, and then in 30% H_2SO_4 solution for 3 h to cleave the hydrogen bonds between cellulose molecules, which resulted in swelling of CMFs.[30] Each piece of CMFs was expanded to 1.30 cm × 1.21 cm × 0.64 cm, almost 10-fold of the volume of the compressed CMFs. After swelling, the CMFs were washed with copious amounts of water. The CMF-supported submicrometer TiO_2 particles were synthesized through the hydrolysis of $(NH_4)_2{\cdot}TiF_6$[55] in the presence of CMFs. Briefly, the swollen CMFs were immersed in an aqueous solution containing $(NH_4)_2{\cdot}TiF_6$ (0.1 M) and H_3BO_3 (0.3 M). The mixture was sonicated for 15 min and then left undisturbed at 70 °C for 3 h. The resulting TiO_2/CMFs composite materials were carefully washed with water to remove unreacted $(NH_4)_2{\cdot}TiF_6$ and H_3BO_3. The TiO_2@Ag/CMFs were synthesized by further growing Ag nanoparticles on the surfaces of CMF-supported TiO_2. In a typical procedure, the TiO_2/CMFs were immersed in 25 mL of glucose solution (4 wt %) at 60 °C for 10 min. The growth of Ag nanoparticles was initiated by adding 10 mL of $AgNO_3$ solution (0.2 M). The temperature of the reaction mixture was maintained at 90 °C for 1 h. The resulting TiO_2@Ag/CMFs were carefully washed with water and finally stored in water for future use.

2.3. Materials Characterizations. A JEOL JEM-2100 transmission electron microscope operated at an accelerating voltage of 200 kV was used for transmission electron microscopy (TEM) imaging of nanoparticle samples drop-dried on 300 mesh Formvar/carbon-coated Cu grids. A Hitachi S-4800 field emission scanning electron microscope was used for scanning electron microscopy (SEM) imaging and energy dispersive spectroscopy (EDS) elemental mapping. The samples were sputter-coated with a nominally 2 nm thick Au film to increase the conductivity for SEM imaging. UV−vis diffuse reflectance spectra were collected using a Hitachi UV-3000 UV−vis spectrophotometer. Powder X-ray diffraction (PXRD) patterns were recorded using a Bruker D8 Advanced X-ray diffractometer with Cu Kα radiation (λ = 0.1542 nm). The contact angles were measured using the image of a sessile drop at the points of intersection between the drop contour and the sample surface, preformed on an Attention KSV CM200 surface tensiometer.

2.4. Monitoring the Photocatalytic Reactions Using UV−Vis Absorption Spectroscopy. The photocatalytic activity of TiO_2@Ag/CMFs was evaluated using photodegradation of 4-CP as a model reaction. In a typical procedure, 100 mg of TiO_2@Ag/CMFs was dispersed into a 200 mL of 4-CP (50 mg L^{-1}) aqueous solution. The pH value of 4-CP solution was carefully adjusted to 4 by adding HCl. The dispersion was kept in dark under magnetic stir for 2 h to establish an adsorption/desorption equilibrium. The photocatalytic reactions were carried out in a GHX-2 photochemical reactor using a mercury lamp (250 W) as the excitation source. The temperature of the reaction was maintained at 25 ± 0.2 °C using circulating water. Air was bubbled through the reaction solution from the bottom at a flow rate of 250 mL min^{-1} to ensure thorough mixing of the molecules and the photocatalysts. During the reactions, aliquots (3 mL) were withdrawn from the reaction mixture every 30 min, and UV−vis absorption spectra were collected on solution samples using a

DOI: 10.1021/acs.iecr.8b00006
Ind. Eng. Chem. Res. 2018, 57, 4277−4286

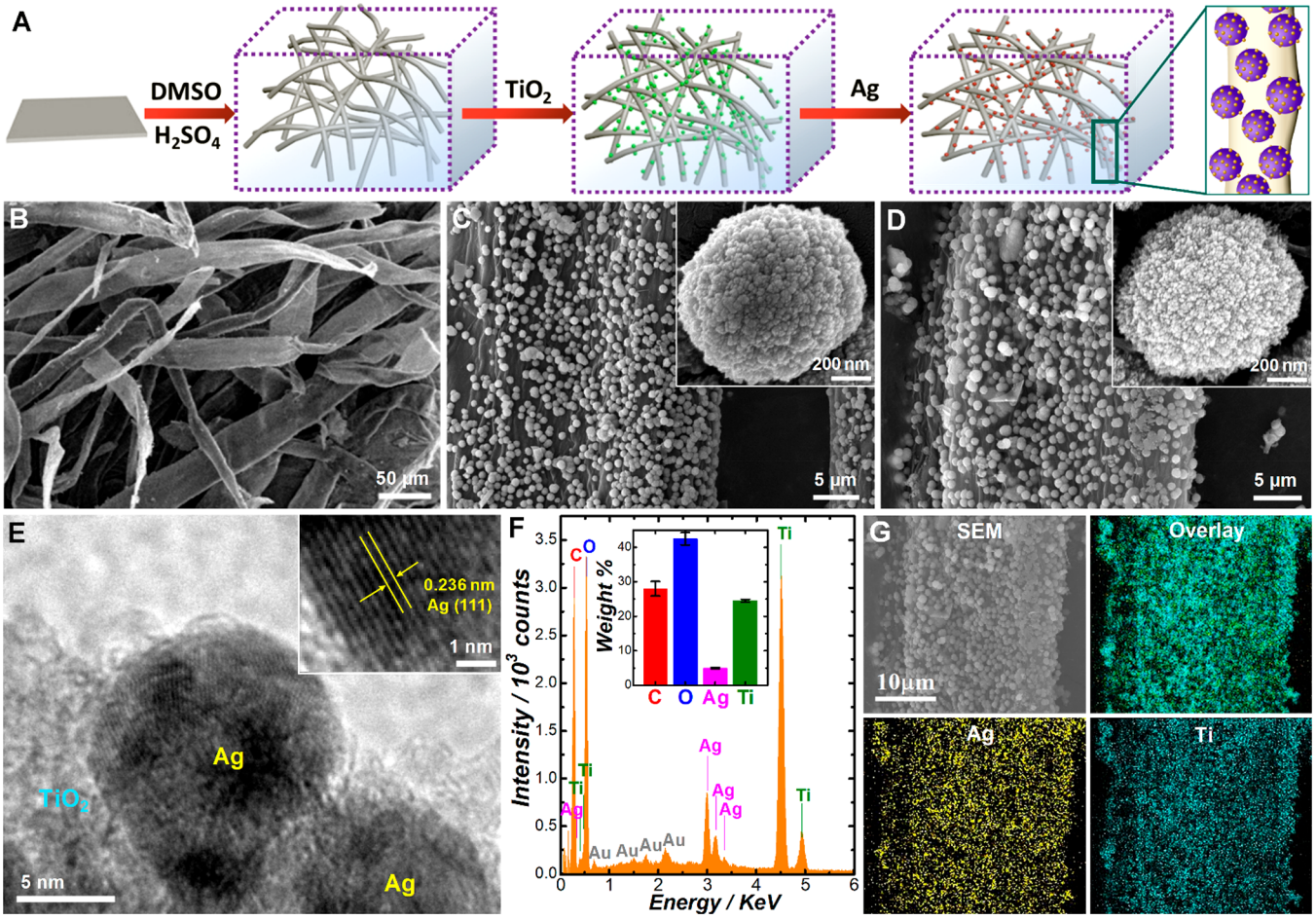

Figure 1. (A) Scheme illustrating the assembly of TiO_2@Ag/CMFs. SEM images of (B) swollen CMFs, (C) TiO_2/CMFs, and (D) TiO_2@Ag/CMFs. The insets in panels C and D are higher magnification SEM images of an individual TiO_2 particle and TiO_2@Ag particle grafted on the CMFs. (E) HRTEM image showing the structures of Ag nanoparticles grafted on the TiO_2 surface. The inset is a HRTEM image showing the (111) lattice spacing of a Ag nanoparticle. (F) EDS spectrum of TiO_2@Ag/CMFs. The inset shows the weight percentages of C, O, Ag, and Ti in the TiO_2@Ag/CMFs. The error bars represent the standard deviations obtained from three samples synthesized following the same protocol. (G) SEM image and spatial distributions of Ag and Ti elements mapped by EDS.

Hitachi UV-3000 UV−vis spectrophotometer after separating the molecules form the photocatalysts through centrifugation.

2.5. Monitoring the Photocatalytic Reactions Using SERS. Substrates of TiO_2@Ag/CMFs with dimensions of 1.30 cm × 1.21 cm × 0.64 cm were immersed in 20 mL of 50 mg L^{-1} of 4-CP solution in dark and left undisturbed for 2 h. Each TiO_2@Ag/CMF substrate was then carefully rinsed with copious amounts of water and placed in a well of a six-hole white spot plate. 2 mL of water was added to each well to prevent the substrates from drying during the SERS measurements. SERS spectra were collected using a Renishaw inVia confocal Raman microscope equipped with a continuous wave diode excitation laser at 532 nm. A 50×, 0.50 NA Leica objective with a long working distance was used to focus the excitation beam onto the sample with a focal spot size of ∼2 μm. The laser power focused on the samples was 1 mW, and the spectral acquisition time was 30 s. To monitor the photocatalytic degradation of 4-CP *in situ*, the laser was focused on a particular spot on the photocatalysts to collect SERS signals in real time during the reactions. An UVA LED lamp (365 nm, Labino) was used as the excitation source for the photocatalytic reactions. The distance between the lamp and the photocatalyst substrates was 38 cm, and the power density of UV light irradiated on the laser-focused spot was 25 mW cm^{-2}. Normal Raman spectra of various molecules were collected on solid state samples supported by silicon wafers under 532 nm excitation with 1 mW excitation power and 30 s spectral acquisition time. Raman peak assignments were accomplished based on density functional theory (DFT) calculations using the Gaussian 03 software package. The molecular structures were optimized, and their Raman frequencies were calculated with Becke's hybrid functional, B3LYP, at the 6-311G** level. The harmonic frequencies were determined by the Hessian diagonalization, and the Raman activities were determined by polarization. A single scaling factor of 0.956 was used to calibrate the calculated frequencies. The calculated spectra were originally composed of spectral spikes at the characteristic vibrational frequencies, and Lorentzian was used to expand the calculated differential Raman scattering cross sections with a wavenumber interval of 10 cm^{-1}.

3. RESULTS AND DISCUSSION

3.1. Synthesis and Characterizations of TiO_2@Ag/CMFs. Figure 1A schematically illustrates the key steps involved in the synthesis of TiO_2@Ag/CMFs. Swollen CMFs were chosen as the substrates to support photocatalytically

DOI: 10.1021/acs.iecr.8b00006
Ind. Eng. Chem. Res. 2018, 57, 4277−4286

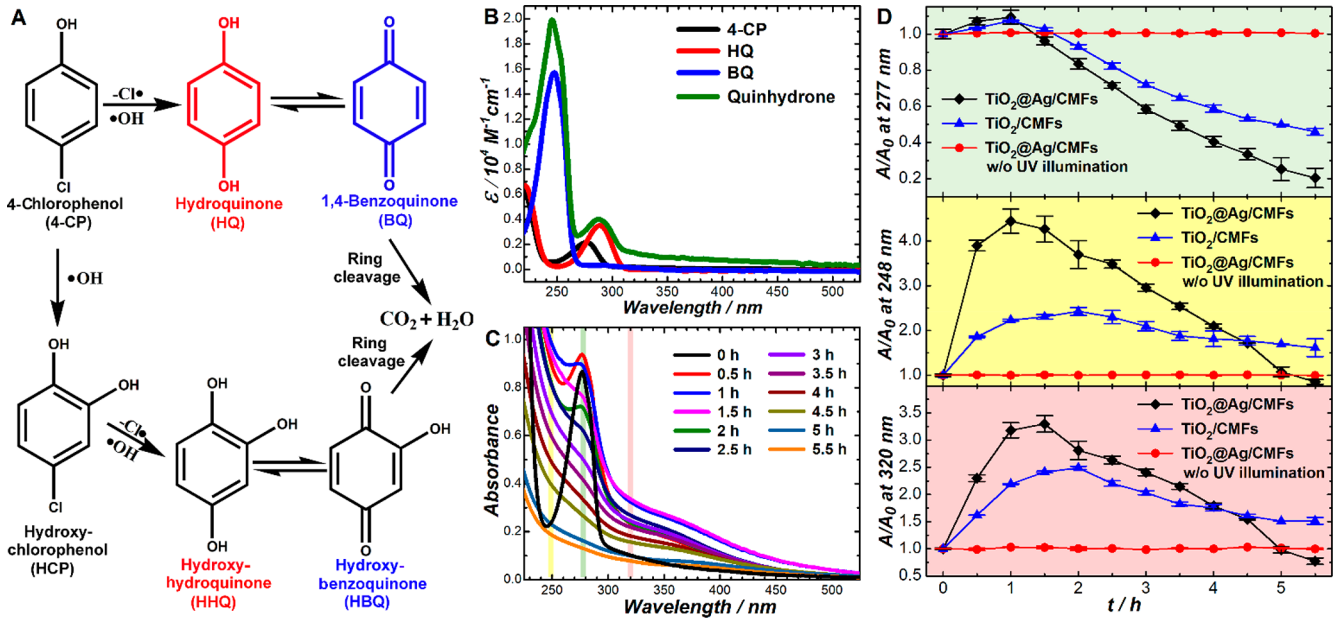

Figure 2. (A) Schematic illustration of the pathways involved in the photocatalytic degradation of 4-CP. (B) UV−vis absorption spectra of 4-CP, HQ, BQ, and quinhydrone aqueous solutions. (C) Temporal evolution of UV−vis absorption spectra of the reaction mixtures during the photocatalytic degradation of 4-CP on TiO_2@Ag/CMFs. (D) Temporal evolution of normalized absorbance, A/A_0, at 277, 248, and 320 nm during the photocatalytic degradation of 4-CP on TiO_2@Ag/CMFs and TiO_2/CMFs. The temporal evolution of A/A_0 in the presence of TiO_2@Ag/CMFs without UV light illumination was also shown for comparison. A_0 is the absorbance before the reaction, and A is the absorbance at particular reaction times. The error bars represent the standard deviations obtained from three experimental runs.

active TiO_2@Ag nanocomposite particles because of their low cost, structural robustness, easy processability, and highly hydrophilic open surfaces accessible by the reactant molecules. The commercial cellulose paper was composed of compressed CMFs, which underwent a swelling process upon acid hydrolysis in 30% H_2SO_4, resulting in volume expansion by approximately 10 times. The swelling of the compressed CMFs gave rise to drastic increase in the mass-specific surface areas and high abundance of hydrophilic surface functional groups, such as −COOH, −CO, and −OH, both of which were highly desired for the subsequent nanoparticle nucleation and growth as well as photocatalytic 4-CP mineralization in aqueous environments. The swollen CMF networks consisted of 20−50 μm microfibers (Figure 1B), whose surfaces became densely decorated with submicrometer TiO_2 particles (Figure 1C) after the CMF surface-mediated $(NH_4)_2{\cdot}TiF_6$ hydrolysis. Each submicrometer TiO_2 particle was essentially composed of densely packed primary nanocrystals that were 20−40 nm in size and exhibited a highly roughened surface morphology (inset of Figure 1C). After Ag nanocrystals were further grown on the surfaces of CMF-supported TiO_2 particles, the particle surfaces became even rougher (Figure 1D). The TiO_2 particles were 848 ± 119 nm in diameter, while the Ag nanoparticles were only 10.9 ± 2.4 nm in size (Figure S1 in Supporting Information). More detailed structural information on the Ag nanoparticles deposited on the TiO_2 surfaces was obtained from high-resolution TEM (HRTEM) images (Figure 1E). The characteristic (111) lattice fringes of face-centered cubic (fcc) Ag with a spacing of 2.36 Å were clearly resolved (inset of Figure 1E). Each Ag nanocrystal was quasi-spherical in shape with a multitwinned crystalline structure (Figure S2).

The structures and compositions of TiO_2@Ag/CMFs were further characterized by PXRD and EDS elemental analysis. PXRD results (Figure S3) clearly showed that the as-constructed TiO_2@Ag/CMFs were composed of three crystalline components, crystalline cellulose (JCPDS no. 00-050-2241), anatase phase of TiO_2 (JCPDS no. 01-071-1166), and fcc phase of Ag (JCPDS no. 00-001-1164). As quantified by EDS, the weight % of C, O, Ag, and Ti in the TiO_2@Ag/CMFs composites were 28.0, 42.5, 5.0, and 24.5%, respectively (Figure 1F). The Au signals in the EDS originated from the 2 nm thick Au film sputter-coated on the samples for SEM imaging. Correlated SEM imaging and EDS elemental mapping showed that both Ag and Ti elements were uniformly distributed over the CMF surfaces (Figure 1G). We also used SEM and EDS to characterize free-standing TiO_2/Ag nanocomposite particles peeled off from the CMF supports (Figure S4), which further confirmed that the surface of each TiO_2 particle was densely decorated with Ag nanoparticles.

We used UV−vis diffuse reflectance spectroscopy to characterize the optical properties of TiO_2/CMFs and TiO_2@Ag/CMFs (Figure S5). The TiO_2/CMFs strongly absorbed light in the UV and exhibited a band gap energy of 3.22 eV, which was in excellent agreement with the band gap of bulk anatase.[56] When the CMF-supported TiO_2 particles were decorated with Ag nanocrystals, an additional broad absorption band emerged spanning the entire visible spectral range, which originated from the strong plasmonic coupling between the Ag nanoparticles grafted on the TiO_2 particle surfaces. While colloidal Ag nanoparticles around 10 nm in size typically exhibit a sharp plasmon-dominated optical extinction peak below 400 nm, the plasmonic coupling between Ag nanoparticles in close proximity leads to significant spectral red-shift and line shape broadening of the plasmon resonance bands.[57] Such plasmonic coupling also produces enormous field enhancements in the interparticle gaps, which serve as the hot spots for SERS under visible laser excitations.[57] As demonstrated in greater detail later in this paper, the plasmon coupling among Ag nanoparticles on the TiO_2 particle surfaces generated high density of hot spots at the molecule−photocatalyst interfaces, enabling us to probe the

DOI: 10.1021/acs.iecr.8b00006
Ind. Eng. Chem. Res. 2018, 57, 4277−4286

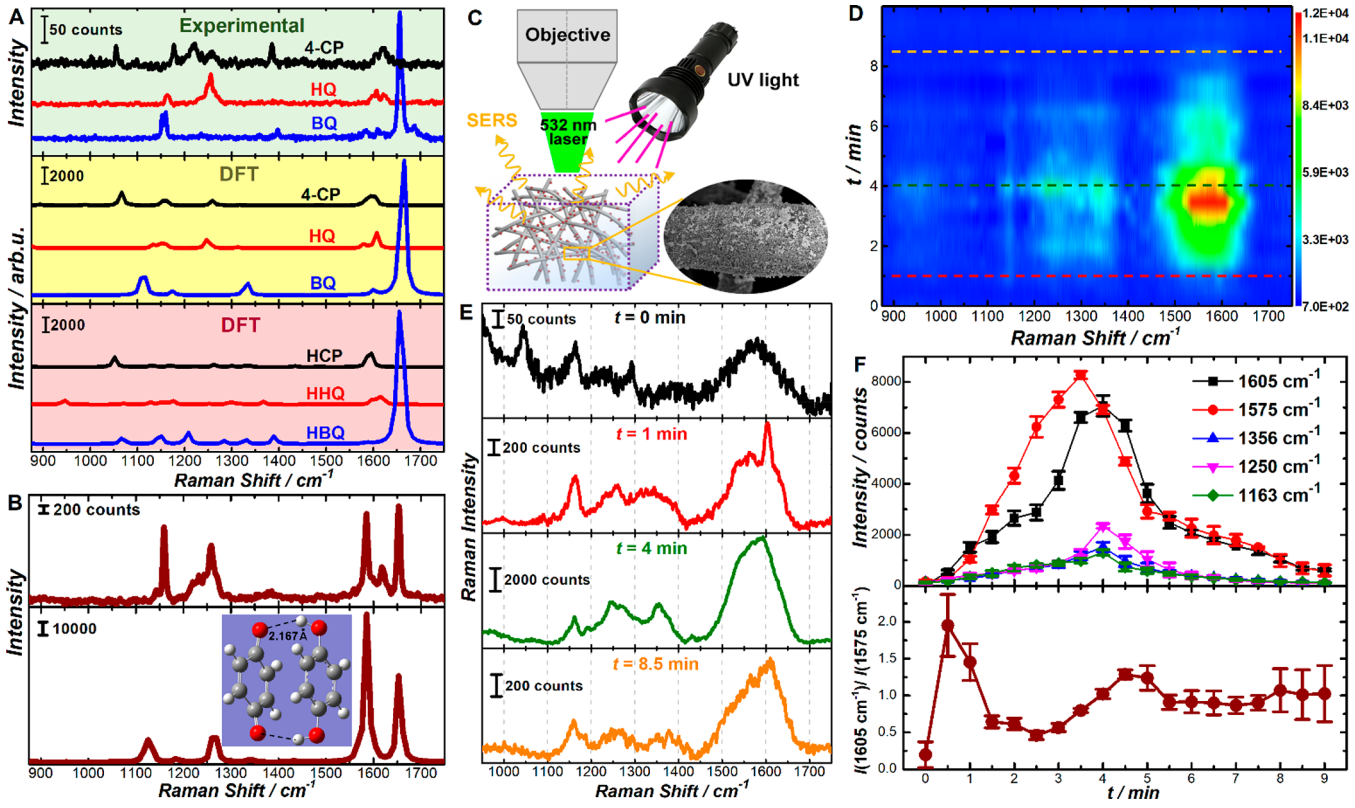

Figure 3. (A) (top panel) Experimentally measured normal Raman spectra of 4-CP, HQ, and BQ, (middle panel) calculated Raman spectra of 4-CP, HQ, and BQ, and (bottom panel) calculated Raman spectra of HCP, HHQ, and HBQ using DFT. The spectra are offset for clarity. (B) (upper panel) Experimentally measured normal Raman spectrum and (bottom panel) DFT-calculated Raman spectrum of quinhydrone. (C) Schematic illustration of SERS-based *in situ* reaction monitoring. (D) Temporal evolution of SERS spectra during the photocatalytic degradation of 4-CP on TiO_2@Ag/CMFs. (E) Snapshot SERS spectra at reaction times of 0, 1, 4, and 8.5 min. (F) Temporal evolution of (upper panel) SERS peak intensities of the Raman modes at 1605, 1575, 1356, 1250, and 1163 cm^{-1} and (bottom panel) intensity ratio between the 1605 and 1575 cm^{-1} modes during the photocatalytic reaction. The error bars represent the standard deviations obtained from three experimental runs.

photocatalytic interfacial molecular transformations using SERS.

3.2. Photocatalytic Degradation of 4-CP on TiO_2@Ag/CMFs. Although many aspects regarding the detailed mechanisms of the 4-CP degradation on TiO_2 photocatalysts under UV illumination still remain ambiguous and open to further scrutiny, a consensus has been reached that the primary degradation pathway involves a series of hydroxylation (mediated by hydroxyl radicals), dechlorination, dehydrogenation, and aromatic ring cleavage steps,[7,8,10,11] as schematically illustrated in Figure 2A. HQ and BQ have been identified as two major intermediates along this reaction pathway.[7,8,10,11] HQ and BQ are interconvertible and can further form a HQ/BQ charge-transfer complex known as quinhydrone.[58] The charge transfer between the HQ and BQ units in the quinhydrone complex has long been of great interests to both the electrochemistry and photochemistry communities.[59−63] Also illustrated in Figure 2A is a secondary reaction pathway involving several further hydroxylated intermediates, such as hydroxychlorophenol (HCP), hydroxyhydroquinone (HHQ), and hydroxybenzoquinone (HBQ).[9] While a series of other intermediates may also form during the photocatalytic degradation of 4-CP depending on the pH of the reaction medium and detailed surface structures of the TiO_2 photocatalysts,[7] HQ, BQ, and their hydroxylated derivatives (HHQ and HBQ) are generally considered to be the final aromatic intermediates before the ring cleavage.[7−11]

The mechanistic complexity of photocatalytic degradation of 4-CP was fully reflected by the temporal evolution of UV−vis absorption spectral features during the reactions. As shown in Figure 2B, 4-CP, HQ, and BQ exhibited distinct absorption spectral features in terms of peak positions, line shapes, and intensities. We measured the wavelength-dependent absorbance, A, of aqueous solutions of 4-CP, HQ, and BQ at pH of 4 and then converted the absorbance into molar absorptivity, ε, using the Lambert−Beer's law to quantitatively compare the absorption cross sections of the molecules. 4-CP showed an absorption peak centered at ~277 nm with an ε value of 2.1×10^3 M^{-1} cm^{-1}, which was attributed to the n → π^* electron transitions coupling the lone pair electrons of hydroxyl oxygen with the π electrons of the aromatic ring. When 4-CP was converted into HQ, the major absorption peak shifted to ~288 nm, exhibiting an ε value of 2.5×10^3 M^{-1} cm^{-1} at the peak position. The strongest absorption band of BQ was centered at 248 nm with an ε value of 1.56×10^4 M^{-1} cm^{-1}, which was assigned to the $\pi \rightarrow \pi^*$ electron transition between aromatic ring and oxygen. For comparison, the absorption spectrum of quinhydrone (HQ/BQ heterodimer complex) is also shown in Figure 2B. While the characteristic absorption peaks of monomeric HQ and BQ were both preserved, the charge transfers between the HQ and BQ units in quinhydrone resulted in the emergence of a broad spectral shoulder extending from ~300 nm all the way into the visible spectral region, a spectral feature signifying the charge transfers in both

DOI: 10.1021/acs.iecr.8b00006
Ind. Eng. Chem. Res. 2018, 57, 4277−4286

quinhydrone and quinhydrone-type $\pi-\pi$ stacking complexes.[64−66] Because of the similarity in spectral features, it remained impossible, however, to further distinguish HCP, HHQ, and HBQ from 4-CP, HQ, and BQ, respectively, using UV−vis absorption spectroscopy.

The as-synthesized TiO_2@Ag/CMFs exhibited superhydrophilic surfaces (Figure S6), which was highly desired for heterogeneous photocatalysis in aqueous environments. After incubating the TiO_2@Ag/CMFs with 4-CP aqueous solution for 2 h, an adsorption/desorption equilibrium was established, resulting in a saturated surface loading of 1.88 mg of 4-CP in 100 mg of TiO_2@Ag/CMFs matrix as quantified by UV−vis absorption spectroscopy (Figure S7). The detailed spectral evolution (Figure 2C) suggested that HQ, BQ, and quinhydrone all emerged as intermediates during the photocatalytic degradation of 4-CP. We qualitatively tracked the kinetic trajectories of 4-CP based on the temporal evolutions of the absorbance at 277 nm (top panel in Figure 2D). The absorbance at 277 nm increased during the first hour upon initiation of photocatalytic reaction because of the spectral overlap between the absorption peaks of 4-CP and HQ at this wavelength. As the reaction further proceeded, the absorbance at 277 nm progressively decreased due to the conversion of HQ into BQ and the subsequent aromatic ring cleavage. The temporal evolution of the absorbance at 248 nm (middle panel in Figure 2D) and 320 nm (bottom panel in Figure 2D) qualitatively reflected the concentration evolutions of BQ and quinhydrone, respectively. Without UV illumination, no reaction occurred, confirming that the degradation of 4-CP was essentially a photocatalytic process rather than a thermal reaction. The photodegradation of 4-CP on TiO_2/CMFs was observed to be significantly slower than that on TiO_2@Ag/CMFs (Figure 2D and Figure S8), suggesting that Ag nanoparticles further enhanced the intrinsic photocatalytic activity of TiO_2 by serving as efficient electron sinks to boost the hole-driven reactions.[67−70] The TiO_2@Ag/CMFs photocatalyst could be recycled through a simple centrifugation-UV cleaning procedure, and its catalytic activity was well-preserved over multiple consecutive reaction cycles (Figure S9).

Although UV−vis absorption spectroscopy provided a straightforward way to obtain qualitative kinetic profiles of the photocatalytic reactions, kinetic studies at more detailed and quantitative levels remained challenging due to the spectral overlaps between the reactant and multiple intermediates. In addition, UV−vis absorption spectroscopy was incapable of resolving the intrinsic kinetics of molecular transformations at the molecule−photocatalyst interfaces without the complications introduced by molecular adsorption, desorption, and diffusion. Furthermore, UV−vis absorption spectroscopy did not provide detailed molecular fingerprinting information in real time, preventing us from being able to identify the intermediates reflecting the kinetic bottlenecks along the reaction pathways. To further shed light on the detailed reaction mechanisms, we used SERS as an *in situ* spectroscopic tool to resolve the temporal evolution of detailed molecular structures at the molecule−photocatalyst interfaces.

3.3. *In Situ* Reaction Monitoring Using SERS. Raman spectroscopy provided remarkably more detailed information on molecular structures than UV−vis absorption spectroscopy, making it possible to spectroscopically distinguish 4-CP, HQ, BQ, and quinhydrone. As demonstrated previously, the use of SERS as an *in situ* plasmon-enhanced spectroscopic tool enabled identification of important transient intermediates along the pathways of surface-catalyzed molecular transformations.[48−51] The top panel in Figure 3A showed the normal Raman spectra of 4-CP, HQ, and BQ, all of which exhibited a characteristic Raman peak corresponding to the aromatic ring C═C stretching mode centered at 1619, 1621, and 1610 cm^{-1}, respectively. Several other characteristic Raman peaks corresponding to the C−O stretching, C−H in-plane bending, and C−Cl stretching modes were also observed in the spectral range of 1000−1400 cm^{-1}. The strongest Raman peak of BQ located at ∼1657 cm^{-1} was assigned to the C═O stretching mode coupled with the aromatic ring and had a Raman cross section about 10 times higher than those of the aromatic ring C═C stretching modes. The assignments of the major Raman peaks are listed in Table S1 of the Supporting Information. We also calculated the Raman spectra of 4-CP, HQ, and BQ through DFT calculations (middle panel of Figure 3A). The calculated spectra matched the experimental spectra reasonably well, which further confirmed our peak assignments. DFT calculations also showed that HCP, HHQ, and HBQ exhibited Raman spectral features very similar to those of 4-CP, HQ, and BQ, respectively (bottom panel of Figure 3A). Therefore, it still remained challenging to further distinguish 4-CP, HQ, and BQ from their hydroxylated derivatives using SERS.

For the quinhydrone complex, the spectral cross section of the C═C aromatic ring mode was drastically amplified, becoming commensurate with that of the C═O stretching mode essentially due to the coupling between the HQ and BQ units (upper panel of Figure 3B). The formation of quinhydrone complex also resulted in remarkable enhancements of both the C−H in-plane bending and C−O stretching modes in comparison to those of HQ, whereas the O−H stretching modes became significantly broadened as a consequence of hydrogen bonding between HQ and BQ. All these experimentally observed spectral features were well reproduced by DFT calculations (lower panel of Figure 3B). The molecular structures of quinhydrone optimized by DFT calculations (inset of the lower panel of Figure 3B) showed that the bond length of the O−H bond bridging the HQ and BQ units was 2.167 Å, in excellent agreement with a previous prediction.[59] The distinct Raman signatures and spectral cross sections of 4-CP, HQ, BQ, and quinhydrone enabled us to use SERS to precisely monitor the detailed molecular structural evolutions and unambiguously identify the key reaction intermediates during the photocatalytic degradation of 4-CP.

We used the TiO_2@Ag/CMFs as both the photocatalysts and SERS substrates to spectroscopically monitor the photocatalytic degradation of 4-CP in real time (see schematic illustration in Figure 3C). The TiO_2@Ag/CMFs loaded with 4-CP were exposed to UV illumination (365 nm, 25 mW cm^{-2}) to generate photoexcited electrons and holes in the TiO_2, which drove the photocatalytic reactions. SERS spectra were collected using a confocal Raman microscope under visible excitation at 532 nm with an excitation power density of ∼32 kW cm^{-2} at the focal point, which was in the typical excitation power range for SERS measurements. The excitation of the plasmon resonances of Ag in the visible spectral range generated plasmonic hot electrons, which might also be harnessed to drive interesting photocatalytic reactions along unconventional pathways distinct form those involved in the semiconductor-based photocatalysis.[71−74] However, illumination by the visible laser alone without UV irradiation did not result in any observable degradation of 4-CP or other reactions

DOI: 10.1021/acs.iecr.8b00006
Ind. Eng. Chem. Res. 2018, 57, 4277−4286

(Figure S10), indicating that the photocatalytic degradation of 4-CP observed under the current experimental conditions was essentially driven by the photoexcited charge carriers in TiO_2 rather than the plasmonic hot electrons in Ag.

The time-resolved SERS spectra during the photocatalytic degradation of 4-CP on the TiO_2@Ag/CMFs are shown in Figure 3D, and several snapshot spectra at various stages of the reaction are highlighted in Figure 3E. The molecular transformations during the photocatalytic reactions were tracked based on the temporal evolution of the characteristic vibrational modes of the molecules in the SERS spectra in the spectral range from 950 to 1750 cm^{-1}, while the spectral features at lower wavenumbers (200−800 cm^{-1}) were essentially dominated by the characteristic Raman modes of the anatase phase of TiO_2 (Figure S11). The Raman modes corresponding to the C−Cl stretching, O−H stretching, C−O stretching, C−H in-plane bending, aromatic ring C═C stretching, and C═O stretching modes were all clearly resolved in the SERS spectra. In comparison to the normal Raman peaks, the SERS peaks of the same vibrational modes were observed to be significantly broadened and shifted within certain spectral ranges due to the interactions between the molecular adsorbates and the photocatalyst surfaces as well as the heterogeneity associated with molecular orientations with respect to the photocatalyst surfaces. The assignments of the major SERS peaks are listed in Table S1.

By tracking the temporal evolutions of five major SERS peaks during the reactions (upper panel of Figure 3F), we were able to gain important mechanistic insights into the multistep molecular transformations involved in the photocatalytic degradation of 4-CP. A series of interesting phenomena were observed. First, the formation of HQ through dechlorination and hydroxylation of 4-CP was a kinetically fast step occurring at the initial stage of the photocatalytic degradation. The characteristic SERS peak of the C−Cl stretching mode (1048 cm^{-1}) completely disappeared accompanied by the spectral downshifts of both the O−H stretching (from 1390 to 1356 cm^{-1}) and C−O stretching (from 1295 to 1250 cm^{-1}) modes within 1 min upon the initiation of the photocatalytic reactions. Second, the *in situ* generated HQ underwent a rapid oxidation process to form BQ, which was evident by the emergence of the SERS peak of C═O stretching mode at 1605 cm^{-1} and the enhancement of the C−H in-plane bending mode around 1163 cm^{-1}. Third, HQ and BQ further reacted with each other to form quinhydrone, whose Raman cross sections of the O−H stretching, C−O stretching, C−H in-plane bending, and aromatic ring C═C stretching modes were all about 1 order of magnitude higher than those of the monomeric HQ and BQ due to the charge transfers in the dimeric complex. As a consequence, the intensities of several SERS modes were observed to increase simultaneously upon the formation of quinhydrone, though the plasmonic field enhancements provided by the Ag nanoparticles remained essentially unchanged. Fourth, all the SERS peaks clearly resolvable in this case were associated with the aromatic ring. Once the aromatic compounds underwent ring cleavage, the intensities of the SERS peaks dropped drastically and became vanishingly weak after complete ring cleavage. Fifth and most interestingly, the dimeric quinhydrone complex was identified to be the final aromatic intermediates before the formation of mineralization products upon ring cleavage. While the Raman cross section of the C═O stretching mode of BQ was about 10 times larger than that of the aromatic ring C═C stretching mode of HQ, the two modes became almost equally strong upon the formation of quinhydrone (Figure 3B). Therefore, the temporal evolution of the intensity ratio between the 1605 and 1575 cm^{-1} modes, $I(1605\ cm^{-1})/I(1575\ cm^{-1})$, could be used to track the formation and consumption of quinhydrone during the multistep reactions (lower panel of Figure 3F). To more quantitatively evaluate the relative peak intensities of the two Raman modes, we performed peak deconvolution to decompose the spectral features into two peaks centered at 1605 and 1575 cm^{-1}, respectively, using the Origin 7.5 software package (Figure S12). At the initial stage of the photocatalytic reactions (within 1 min), a rapid increase of $I(1605\ cm^{-1})/I(1575\ cm^{-1})$ was observed due to the conversion of HQ into BQ. Upon the formation of quinhydrone, $I(1605\ cm^{-1})/I(1575\ cm^{-1})$ started to decrease until reaching a steady state value around 1 after 4 min. At the same time, the peak intensities of several other Raman modes also reached their maxima, strongly indicating that the majority of monomeric HQ and BQ were complexed into the dimeric quinhydrone. As the reactions further proceeded, all the SERS peaks became weaker due to the aromatic ring cleavage. However, the $I(1605\ cm^{-1})/I(1575\ cm^{-1})$ still remained around 1, strongly indicating that quinhydrone rather than the monomeric HQ, BQ, or their further hydroxylated derivatives (HHQ and HBQ) served as the final aromatic intermediate species prior to the ring cleavage. Our time-resolved SERS results provided experimental evidence that quinhydrone served as a short circuit for photocatalytic degradation of 4-CP.

4. CONCLUSIONS

As exemplified by this work, the incorporation of spectroscopy-based molecular characterization functionality into photocatalytically active materials systems enables *in situ* monitoring of detailed interfacial molecular transformations during photocatalytic reactions. We have assembled a hierarchical suprastructure consisting of CMF-supported TiO_2@Ag nanocomposite particles, which exhibits unique dual functionalities as both heterogeneous photocatalysts and SERS substrates. Using the photocatalytic degradation of 4-CP on TiO_2@Ag/CMFs as a model reaction system, we have demonstrated that the interfacial chemical transformations on the photocatalyst surfaces can be tracked in real time with detailed molecular structural information using SERS as a time-resolving and molecular fingerprinting spectroscopic tool. Through time-resolved SERS measurements, we have been able to track the temporal evolution of several important aromatic intermediates during the photocatalytic degradation of 4-CP. A key insight gained form our SERS results is that the quinhydrone complex rather than the monomeric HQ, BQ, or their hydroxylated derivatives, such as HHQ and HBQ, serves as the final aromatic intermediates before the mineralization upon aromatic ring cleavage. The current materials system and methodology may be seamlessly applied to the mechanistic investigations of other photocatalytic reactions because TiO_2 exhibits excellent photocatalytic performances toward a large variety of reactions and Ag possesses highly tunable plasmon resonances and intense local field enhancements exploitable for SERS. This work not only highlights the value of SERS as an ultrasensitive spectroscopic tool for *in situ* reaction monitoring but also provides important design principles that guide us to deliberately construct dual-functional materials systems integrating superior photocatalytic performances and *in situ* molecular sensing functions.

DOI: 10.1021/acs.iecr.8b00006
Ind. Eng. Chem. Res. 2018, 57, 4277−4286

■ ASSOCIATED CONTENT

Supporting Information

The Supporting Information is available free of charge on the ACS Publications website at DOI: 10.1021/acs.iecr.8b00006.

Figures and tables as noted in the text, including PXRD patterns, UV−vis diffuse reflectance spectra, particle size distribution, SEM and HRTEM images, EDS elemental maps, UV−vis absorption spectra, SERS spectra, results of contact angle measurements, and a table listing the Raman peak assignments (PDF)

■ AUTHOR INFORMATION

Corresponding Authors

*E-mail wang344@mailbox.sc.edu. Phone 1-803-777-2203. Fax 1-803-777-9521 (H.W.).

*E-mail xfu@ujs.edu.cn (X.F.).

ORCID

Hui Wang: 0000-0002-1874-5137

Notes

The authors declare no competing financial interest.

■ ACKNOWLEDGMENTS

This contribution was identified by Session Chair Jing Zhao (University of Connecticut) as the Best Presentation in the "Colloidal Metal and Semiconductor Nanostructures: Theory, Synthesis and Application" session of the 2017 ACS Fall National Meeting in Washington, DC. H.W. acknowledges the support by National Science Foundation through a CAREER Award (DMR-1253231) and an EPSCoR RII Track-I Award (OIA-1655740). X.F. acknowledges the support by National Natural Science Foundation of China (51302113) and Natural Science Foundation of Jiangsu Province (BK20130512). X.F. also received funding from the Jiangsu University Study-Abroad Funds (20162673) to support his Visiting Scholarship at University of South Carolina. G.Z. was partially supported by a Graduate Research Grant (15A076) from Jiangsu University. L.C. was partially supported by an Innovation and Entrepreneurship Training Program (201710299016Z) of Jiangsu Province, China.

■ REFERENCES

(1) Gaya, U. I.; Abdullah, A. H. Heterogeneous Photocatalytic Degradation of Organic Contaminants Over Titanium Dioxide: A Review of Fundamentals, Progress and Problems. *J. Photochem. Photobiol., C* **2008**, *9*, 1−12.

(2) Chatterjee, D.; Dasgupta, S. Visible Light Induced Photocatalytic Degradation of Organic Pollutants. *J. Photochem. Photobiol., C* **2005**, *6*, 186−205.

(3) Chen, C. C.; Ma, W. H.; Zhao, J. C. Semiconductor-Mediated Photodegradation of Pollutants Under Visible-Light Irradiation. *Chem. Soc. Rev.* **2010**, *39*, 4206−4219.

(4) Pelaez, M.; Nolan, N. T.; Pillai, S. C.; Seery, M. K.; Falaras, P.; Kontos, A. G.; Dunlop, P. S. M.; Hamilton, J. W. J.; Byrne, J. A.; O'Shea, K.; Entezari, M. H.; Dionysiou, D. D. A Review on the Visible Light Active Titanium Dioxide Photocatalysts for Environmental Applications. *Appl. Catal., B* **2012**, *125*, 331−349.

(5) Herrmann, J. M. Heterogeneous Photocatalysis: State of the Art and Present Applications In Honor of Pr. R.L. Burwell Jr. (1912−2003), Former Head of Ipatieff Laboratories, Northwestern University, Evanston (Ill). *Top. Catal.* **2005**, *34*, 49−65.

(6) Xiao, F. X.; Miao, J. W.; Tao, H. B.; Hung, S. F.; Wang, H. Y.; Yang, H. B.; Chen, J. Z.; Chen, R.; Liu, B. One-Dimensional Hybrid Nanostructures for Heterogeneous Photocatalysis and Photoelectrocatalysis. *Small* **2015**, *11*, 2115−2131.

(7) Theurich, J.; Lindner, M.; Bahnemann, D. W. Photocatalytic Degradation of 4-Chlorophenol in Aerated Aqueous Titanium Dioxide Suspensions: A Kinetic and Mechanistic Study. *Langmuir* **1996**, *12*, 6368−6376.

(8) Li, X. J.; Cubbage, J. W.; Tetzlaff, T. A.; Jenks, W. S. Photocatalytic Degradation of 4-Chlorophenol. 1. The Hydroquinone Pathway. *J. Org. Chem.* **1999**, *64*, 8509−8524.

(9) Li, X. J.; Cubbage, J. W.; Jenks, W. S. Photocatalytic Degradation of 4-Chlorophenol. 2. The 4-Chlorocatechol Pathway. *J. Org. Chem.* **1999**, *64*, 8525−8536.

(10) Pera-Titus, M.; García-Molina, V.; Baños, M. A.; Giménez, J.; Esplugas, S. Degradation of Chlorophenols by Means of Advanced Oxidation Processes: a General Review. *Appl. Catal., B* **2004**, *47*, 219−256.

(11) Descorme, C. Catalytic Wastewater Treatment: Oxidation and Reduction Processes. Recent Studies on Chlorophenols. *Catal. Today* **2017**, *297*, 324−334.

(12) Li, F. B.; Li, X. Z. The Enhancement of Photodegradation Efficiency Using Pt-TiO_2 Catalyst. *Chemosphere* **2002**, *48*, 1103−1111.

(13) Han, A.; Zhang, H.; Lu, D.; Sun, J.; Chuah, G. K.; Jaenicke, S. Efficient Photodegradation of Chlorophenols by BiOBr/$NaBiO_3$ Heterojunctioned Composites Under Visible Light. *J. Hazard. Mater.* **2018**, *341*, 83−92.

(14) Li, X. Y.; Cui, Y. H.; Feng, Y. J.; Xie, Z. M.; Gu, J. D. Reaction Pathways and Mechanisms of the Electrochemical Degradation of Phenol on Different Electrodes. *Water Res.* **2005**, *39*, 1972−1981.

(15) Ki, S. J.; Jeon, K.-J.; Park, Y.-K.; Jeong, S.; Lee, H.; Jung, S.-C. Improving Removal of 4-Chlorophenol Using a TiO_2 Photocatalytic System with Microwave and Ultraviolet Radiation. *Catal. Today* **2017**, *293−294*, 15−22.

(16) van Schrojenstein Lantman, E. M.; Deckert-Gaudig, T.; Mank, A. J. G.; Deckert, V.; Weckhuysen, B. M. Catalytic Processes Monitored at the Nanoscale with Tip-Enhanced Raman Spectroscopy. *Nat. Nanotechnol.* **2012**, *7*, 583−586.

(17) Yang, J. L.; Xu, J.; Ren, H.; Sun, L.; Xu, Q. C.; Zhang, H.; Li, J. F.; Tian, Z. Q. *In Situ* SERS Study of Surface Plasmon Resonance Enhanced Photocatalytic Reactions using Bifunctional Au@CdS Core-Shell Nanocomposites. *Nanoscale* **2017**, *9*, 6254−6258.

(18) Hernandez-Alonso, M. D.; Tejedor-Tejedor, I.; Coronado, J. M.; Anderson, M. A. Operando FTIR Study of the Photocatalytic Oxidation of Methylcyclohexane and Toluene in Air over TiO_2-ZrO_2 Thin Films: Influence of the Aromaticity of the Target Molecule on Deactivation. *Appl. Catal., B* **2011**, *101*, 283−293.

(19) Wang, X. L.; Liu, W. Q.; Yu, Y. Y.; Song, Y. H.; Fang, W. Q.; Wei, D. X.; Gong, X. Q.; Yao, Y. F.; Yang, H. G. Operando NMR Spectroscopic Analysis of Proton Transfer in Heterogeneous Photocatalytic Reactions. *Nat. Commun.* **2016**, *7*, 11918.

(20) Qu, L. L.; Wang, N.; Xu, H.; Wang, W. P.; Liu, Y.; Kuo, L. D.; Yadav, T. P.; Wu, J. J.; Joyner, J.; Song, Y. H.; Li, H. T.; Lou, J.; Vajtai, R.; Ajayan, P. M. Gold Nanoparticles and g-C_3N_4-Intercalated Graphene Oxide Membrane for Recyclable Surface Enhanced Raman Scattering. *Adv. Funct. Mater.* **2017**, *27*, 1701714.

(21) Tong, H.; Ouyang, S. X.; Bi, Y. P.; Umezawa, N.; Oshikiri, M.; Ye, J. H. Nano-Photocatalytic Materials: Possibilities and Challenges. *Adv. Mater.* **2012**, *24*, 229−251.

(22) Nakata, K.; Fujishima, A. TiO_2 Photocatalysis: Design and Applications. *J. Photochem. Photobiol., C* **2012**, *13*, 169−189.

(23) Yu, J. C.; Yu, J. G.; Ho, W. K.; Jiang, Z. T.; Zhang, L. Z. Effects of F- Doping on the Photocatalytic Activity and Microstructures of Nanocrystalline TiO_2 Powders. *Chem. Mater.* **2002**, *14*, 3808−3816.

(24) Liu, S. W.; Yu, J. G.; Jaroniec, M. Tunable Photocatalytic Selectivity of Hollow TiO_2 Microspheres Composed of Anatase Polyhedra with Exposed {001} Facets. *J. Am. Chem. Soc.* **2010**, *132*, 11914−11916.

(25) Ding, J.; Dai, Z.; Qin, F.; Zhao, H. P.; Zhao, S.; Chen, R. Z-Scheme $BiO_{1-x}Br/Bi_2O_2CO_3$ Photocatalyst with Rich Oxygen Vacancy

DOI: 10.1021/acs.iecr.8b00006
Ind. Eng. Chem. Res. 2018, 57, 4277−4286

as Electron Mediator for Highly Efficient Degradation of Antibiotics. *Appl. Catal., B* **2017**, *205*, 281−291.
(26) Dai, Z.; Qin, F.; Zhao, H. P.; Ding, J.; Liu, Y. L.; Chen, R. Crystal Defect Engineering of Aurivillius Bi_2MoO_6 by Ce Doping for Increased Reactive Species Production in Photocatalysis. *ACS Catal.* **2016**, *6*, 3180−3192.
(27) Dai, Z.; Qin, F.; Zhao, H. P.; Tian, F.; Liu, Y. L.; Chen, R. Time-Dependent Evolution of the $Bi_{3.64}Mo_{0.36}O_{6.55}/Bi_2MoO_6$ Heterostructure for Enhanced Photocatalytic Activity *via* the Interfacial Hole Migration. *Nanoscale* **2015**, *7*, 11991−11999.
(28) Tian, F.; Zhao, H. P.; Li, G. F.; Dai, Z.; Liu, Y. L.; Chen, R. Modification with Metallic Bismuth as Efficient Strategy for the Promotion of Photocatalysis: The Case of Bismuth Phosphate. *ChemSusChem* **2016**, *9*, 1579−1585.
(29) Sanchez-Garcia, M. D.; Lagaron, J. M. On the Use of Plant Cellulose Nanowhiskers to Enhance the Barrier Properties of Polylactic Acid. *Cellulose* **2010**, *17*, 987−1004.
(30) Özgür Seydibeyoğlu, M.; Oksman, K. Novel Nanocomposites Based on Polyurethane and Micro Fibrillated Cellulose. *Compos. Sci. Technol.* **2008**, *68*, 908−914.
(31) Hamedi, M. M.; Hajian, A.; Fall, A. B.; Håkansson, K.; Salajkova, M.; Lundell, F.; Wågberg, L.; Berglund, L. A. Highly Conducting, Strong Nanocomposites Based on Nanocellulose-Assisted Aqueous Dispersions of Single-Wall Carbon Nanotubes. *ACS Nano* **2014**, *8*, 2467−2476.
(32) Zhu, H.; Luo, W.; Ciesielski, P. N.; Fang, Z.; Zhu, J. Y.; Henriksson, G.; Himmel, M. E.; Hu, L. Wood-Derived Materials for Green Electronics, Biological Devices, and Energy Applications. *Chem. Rev.* **2016**, *116*, 9305−9374.
(33) Han, F.; Kambala, V. S. R.; Srinivasan, M.; Rajarathnam, D.; Naidu, R. Tailored Titanium Dioxide Photocatalysts for the Degradation of Organic Dyes in Wastewater Treatment: A Review. *Appl. Catal., A* **2009**, *359*, 25−40.
(34) Chen, X.; Mao, S. S. Titanium Dioxide Nanomaterials: Synthesis, Properties, Modifications, and Applications. *Chem. Rev.* **2007**, *107*, 2891−2959.
(35) Campion, A.; Kambhampati, P. Surface-Enhanced Raman Scattering. *Chem. Soc. Rev.* **1998**, *27*, 241−250.
(36) Kneipp, K.; Kneipp, H.; Itzkan, I.; Dasari, R. R.; Feld, M. S. Ultrasensitive Chemical Analysis by Raman Spectroscopy. *Chem. Rev.* **1999**, *99*, 2957−2976.
(37) Willets, K. A.; Van Duyne, R. P. Localized Surface Plasmon Resonance Spectroscopy and Sensing. *Annu. Rev. Phys. Chem.* **2007**, *58*, 267−297.
(38) Moskovits, M. Surface-Enhanced Spectroscopy. *Rev. Mod. Phys.* **1985**, *57*, 783−826.
(39) Sharma, B.; Frontiera, R. R.; Henry, A. I.; Ringe, E.; Van Duyne, R. P. SERS: Materials, Applications, and the Future. *Mater. Today* **2012**, *15*, 16−25.
(40) Li, J. F.; Huang, Y. F.; Ding, Y.; Yang, Z. L.; Li, S. B.; Zhou, X. S.; Fan, F. R.; Zhang, W.; Zhou, Z. Y.; Wu, D. Y.; Ren, B.; Wang, Z. L.; Tian, Z. Q. Shell-Isolated Nanoparticle-Enhanced Raman Spectroscopy. *Nature* **2010**, *464*, 392−395.
(41) Nie, S. M.; Emory, S. R. Probing Single Molecules and Single Nanoparticles by Surface-Enhanced Raman Scattering. *Science* **1997**, *275*, 1102−1106.
(42) Kneipp, K.; Wang, Y.; Kneipp, H.; Perelman, L. T.; Itzkan, I.; Dasari, R.; Feld, M. S. Single Molecule Detection Using Surface-Enhanced Raman Scattering (SERS). *Phys. Rev. Lett.* **1997**, *78*, 1667−1670.
(43) Xu, H. X.; Bjerneld, E. J.; Kall, M.; Borjesson, L. Spectroscopy of Single Hemoglobin Molecules by Surface Enhanced Raman Scattering. *Phys. Rev. Lett.* **1999**, *83*, 4357−4360.
(44) Camden, J. P.; Dieringer, J. A.; Wang, Y. M.; Masiello, D. J.; Marks, L. D.; Schatz, G. C.; Van Duyne, R. P. Probing the Structure of Single-Molecule Surface-Enhanced Raman Scattering Hot Spots. *J. Am. Chem. Soc.* **2008**, *130*, 12616−12617.
(45) Heck, K. N.; Janesko, B. G.; Scuseria, G. E.; Halas, N. J.; Wong, M. S. Observing Metal-Catalyzed Chemical Reactions in Situ Using Surface-Enhanced Raman Spectroscopy on Pd-Au Nanoshells. *J. Am. Chem. Soc.* **2008**, *130*, 16592−16600.
(46) Huang, Y. F.; Zhu, H. P.; Liu, G. K.; Wu, D. Y.; Ren, B.; Tian, Z. Q. When the Signal Is Not from the Original Molecule To Be Detected: Chemical Transformation of para-Aminothiophenol on Ag during the SERS Measurement. *J. Am. Chem. Soc.* **2010**, *132*, 9244−9246.
(47) Huang, J. F.; Zhu, Y. H.; Lin, M.; Wang, Q. X.; Zhao, L.; Yang, Y.; Yao, K. X.; Han, Y. Site-Specific Growth of Au-Pd Alloy Horns on Au Nanorods: A Platform for Highly Sensitive Monitoring of Catalytic Reactions by Surface Enhancement Raman Spectroscopy. *J. Am. Chem. Soc.* **2013**, *135*, 8552−8561.
(48) Xie, W.; Herrmann, C.; Kompe, K.; Haase, M.; Schlucker, S. Synthesis of Bifunctional Au/Pt/Au Core/Shell Nanoraspberries for in Situ SERS Monitoring of Platinum-Catalyzed Reactions. *J. Am. Chem. Soc.* **2011**, *133*, 19302−19305.
(49) Jing, H.; Zhang, Q. F.; Large, N.; Yu, C. M.; Blom, D. A.; Nordlander, P.; Wang, H. Tunable Plasmonic Nanoparticles with Catalytically Active High-Index Facets. *Nano Lett.* **2014**, *14*, 3674−3682.
(50) Zhang, Q. F.; Zhou, Y. D.; Villarreal, E.; Lin, Y.; Zou, S. L.; Wang, H. Faceted Gold Nanorods: Nanocuboids, Convex Nanocuboids, and Concave Nanocuboids. *Nano Lett.* **2015**, *15*, 4161−4169.
(51) Zhang, J. W.; Winget, S. A.; Wu, Y. R.; Su, D.; Sun, X. J.; Xie, Z. X.; Qin, D. Ag@Au Concave Cuboctahedra: A Unique Probe for Monitoring Au-Catalyzed Reduction and Oxidation Reactions by Surface-Enhanced Raman Spectroscopy. *ACS Nano* **2016**, *10*, 2607−2616.
(52) Olaniran, A. O.; Igbinosa, E. O. Chlorophenols and Other Related Derivatives of Environmental Concern: Properties, Distribution and Microbial Degradation Processes. *Chemosphere* **2011**, *83*, 1297−1306.
(53) Czaplicka, M. Sources and Transformations of Chlorophenols in the Natural Environment. *Sci. Total Environ.* **2004**, *322*, 21−39.
(54) Abeish, A. M.; Ang, M.; Znad, H. Enhanced Solar-Photocatalytic Degradation of Combined Chlorophenols Using Ferric Ions and Hydrogen Peroxide. *Ind. Eng. Chem. Res.* **2014**, *53*, 10583−10589.
(55) Liu, S.; Sun, X.; Li, J.-G.; Li, X.; Xiu, Z.; Huo, D. Synthesis of Dispersed Anatase Microspheres with Hierarchical Structures via Homogeneous Precipitation. *Eur. J. Inorg. Chem.* **2009**, *2009*, 1214−1218.
(56) Mo, S. D.; Ching, W. Y. Electronic and Optical Properties of 3 Phases of Titanium Dioxide - Rutile, Anatase, and Brookite. *Phys. Rev. B: Condens. Matter Mater. Phys.* **1995**, *51*, 13023−13032.
(57) Halas, N. J.; Lal, S.; Chang, W. S.; Link, S.; Nordlander, P. Plasmons in Strongly Coupled Metallic Nanostructures. *Chem. Rev.* **2011**, *111*, 3913−3961.
(58) Foster, R. Electron Donor-Acceptor Complexes. *J. Phys. Chem.* **1980**, *84*, 2135−2141.
(59) Tsuzuki, S.; Uchimaru, T.; Ono, T. Origin of Attraction in p-Benzoquinone Complexes with Benzene and p-Hydroquinone. *Phys. Chem. Chem. Phys.* **2017**, *19*, 23260−23267.
(60) Tsuji, Y.; Staykov, A.; Yoshizawa, K. Molecular Rectifier Based on π-π Stacked Charge Transfer Complex. *J. Phys. Chem. C* **2012**, *116*, 2575−2580.
(61) D'Souza, F. Molecular Recognition via Hydroquinone-Quinone Pairing: Electrochemical and Singlet Emission Behavior of 5,10,15-Triphenyl-20-(2,5-Dihydroxyphenyl)Porphyrinato Zinc(II)-Quinone Complexes. *J. Am. Chem. Soc.* **1996**, *118*, 923−924.
(62) Gamboa-Valero, N.; Astudillo, P. D.; Gonzalez-Fuentes, M. A.; Leyva, M. A.; Rosales-Hoz, M. D.; Gonzalez, F. J. Hydrogen Bonding Complexes in the Quinone-Hydroquinone System and the Transition to a Reversible Two-Electron Transfer Mechanism. *Electrochim. Acta* **2016**, *188*, 602−610.
(63) Rafiee, M.; Nematollahi, D. Voltammetry of Electroinactive Species Using Quinone/Hydroquinone Redox: A Known Redox System Viewed in a New Perspective. *Electroanalysis* **2007**, *19*, 1382−1386.

DOI: 10.1021/acs.iecr.8b00006
Ind. Eng. Chem. Res. 2018, 57, 4277−4286

(64) Barone, V.; Cacelli, I.; Crescenzi, O.; d'Ischia, M.; Ferretti, A.; Prampolini, G.; Villani, G. Unraveling the Interplay of Different Contributions to the Stability of the Quinhydrone Dimer. *RSC Adv.* **2014**, *4*, 876−885.
(65) Bouvet, M.; Malezieux, B.; Herson, P. A Quinhydrone-Type 2:1 Acceptor-Donor Charge Transfer Complex Obtained *via* a Solvent-Free Reaction. *Chem. Commun.* **2006**, 1751−1753.
(66) Bouvet, M.; Malezieux, B.; Herson, P.; Villain, F. Self-Organization of the 2-Methoxyquinhydrone Charge Transfer Complex in Polar Planes. *CrystEngComm* **2007**, *9*, 270−272.
(67) Awazu, K.; Fujimaki, M.; Rockstuhl, C.; Tominaga, J.; Murakami, H.; Ohki, Y.; Yoshida, N.; Watanabe, T. A Plasmonic Photocatalyst Consisting of Sliver Nanoparticles Embedded in Titanium Dioxide. *J. Am. Chem. Soc.* **2008**, *130*, 1676−1680.
(68) Hirakawa, T.; Kamat, P. V. Charge Separation and Catalytic Activity of Ag@TiO_2 Core-Shell Composite Clusters Under UV-Irradiation. *J. Am. Chem. Soc.* **2005**, *127*, 3928−3934.
(69) Subramanian, V.; Wolf, E.; Kamat, P. V. Semiconductor-Metal Composite Nanostructures. To What Extent Do Metal Nanoparticles Improve the Photocatalytic Activity of TiO_2 Films? *J. Phys. Chem. B* **2001**, *105*, 11439−11446.
(70) Zhong, X.; Dai, Z.; Qin, F.; Li, J.; Yang, H.; Lu, Z.; Liang, Y.; Chen, R. Ag-Decorated Bi_2O_3 Nanospheres with Enhanced Visible-Light-Driven Photocatalytic Activities for Water Treatment. *RSC Adv.* **2015**, *5*, 69312−69318.
(71) Mukherjee, S.; Libisch, F.; Large, N.; Neumann, O.; Brown, L. V.; Cheng, J.; Lassiter, J. B.; Carter, E. A.; Nordlander, P.; Halas, N. J. Hot Electrons Do the Impossible: Plasmon-Induced Dissociation of H_2 on Au. *Nano Lett.* **2013**, *13*, 240−247.
(72) Manjavacas, A.; Liu, J. G.; Kulkarni, V.; Nordlander, P. Plasmon-Induced Hot Carriers in Metallic Nanoparticles. *ACS Nano* **2014**, *8*, 7630−7638.
(73) Linic, S.; Aslam, U.; Boerigter, C.; Morabito, M. Photochemical Transformations on Plasmonic Metal Nanoparticles. *Nat. Mater.* **2015**, *14*, 567−576.
(74) Kale, M. J.; Avanesian, T.; Christopher, P. Direct Photocatalysis by Plasmonic Nanostructures. *ACS Catal.* **2014**, *4*, 116−128.

DOI: 10.1021/acs.iecr.8b00006
Ind. Eng. Chem. Res. 2018, 57, 4277−4286

Supporting Information for

Cellulose Microfiber-Supported TiO_2@Ag Nanocomposites: A Dual-Functional Platform for Photocatalysis and *in situ* Reaction Monitoring

Guolin Zhang[†], *Long Chen*[†], *Xiaoqi Fu*[*,†], *and Hui Wang*[*,‡]

[†] *School of Chemistry and Chemical Engineering, Jiangsu University, Zhenjiang, Jiangsu 212013, China.*

[‡] *Department of Chemistry and Biochemistry, University of South Carolina, Columbia, South Carolina 29208, United States*

[*] *To whom correspondence should be addressed.*

Email: wang344@mailbox.sc.edu (H. Wang)*; Phone: 1-803-777-2203; Fax: 1-803-777-9521.*

xfu@ujs.edu.cn (X. Fu).

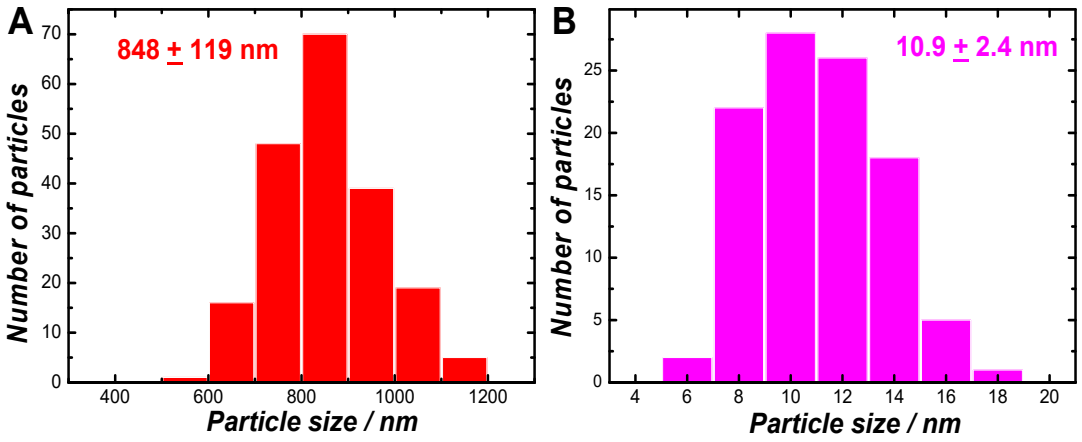

Figure S1. Size distributions of (A) submicron TiO_2 particles and (B) Ag nanoparticles. The particle sizes of TiO_2 and Ag were analyzed on the basis of SEM and TEM images, respectively.

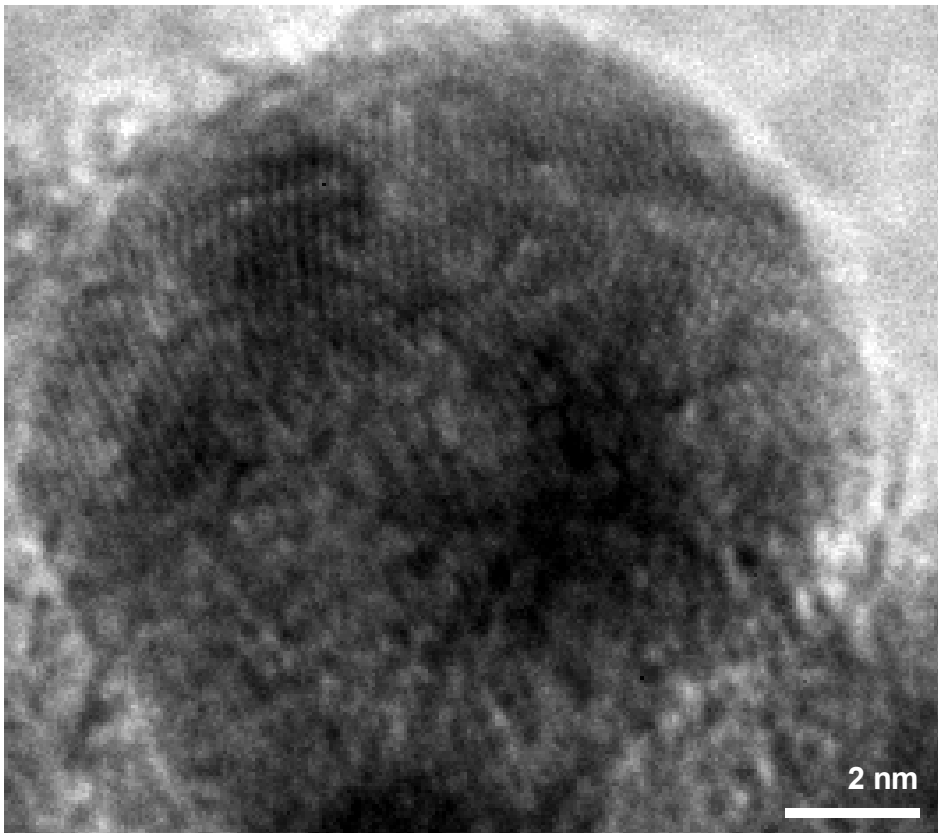

Figure S2. HRTEM image of one Ag nanoparticle on TiO_2.

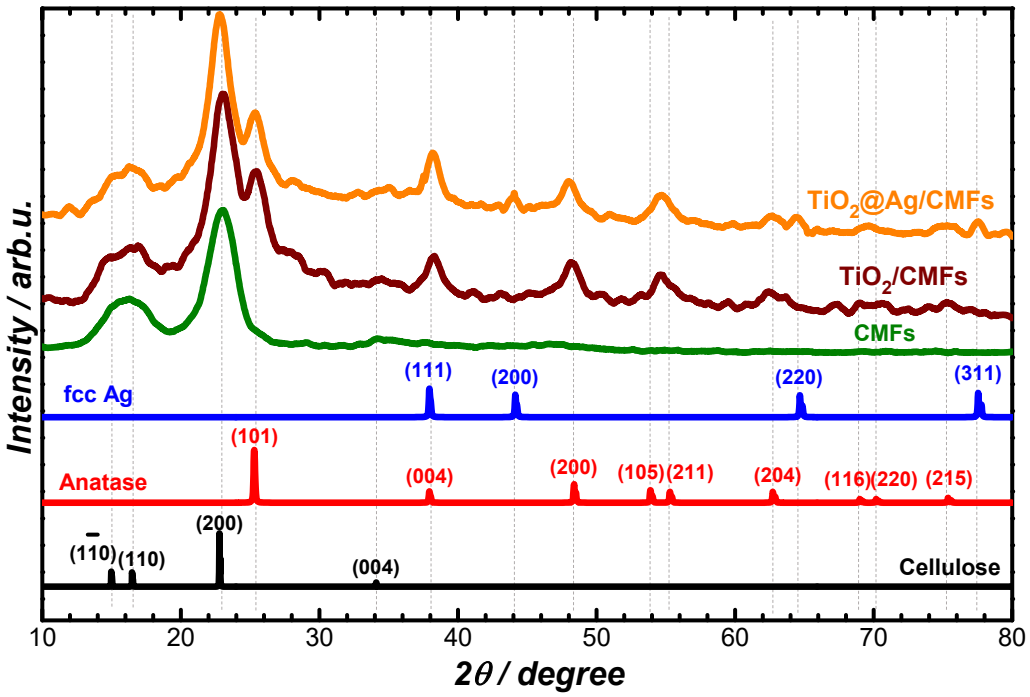

Figure S3. PXRD patterns of CMFs, TiO_2/CMFs, and TiO_2@Ag/CMFs. The standard patterns of bulk cellulose (JCPDS no: 00-050-2241), the anatase phase of TiO_2 (JCPDS no: 01-071-1166), and the face-centered cubic (fcc) phase of Ag (JCPDS no: 00-001-1164) are also shown for comparison. The diffraction patterns are offset for clarity.

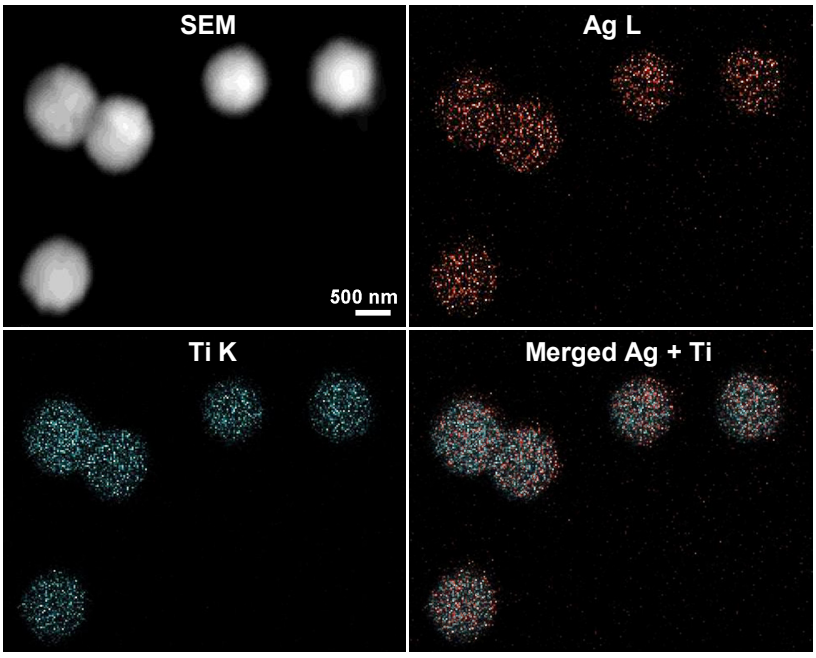

Figure S4. SEM image of TiO_2@Ag nanocomposite particles peeled from the CMF supports and the corresponding EDS elemental distributions of Ag (image of Ag L line intensity at 2.96 keV), Ti (image of Ti K line intensity at 4.51 keV), and merged image of Ag + Ti.

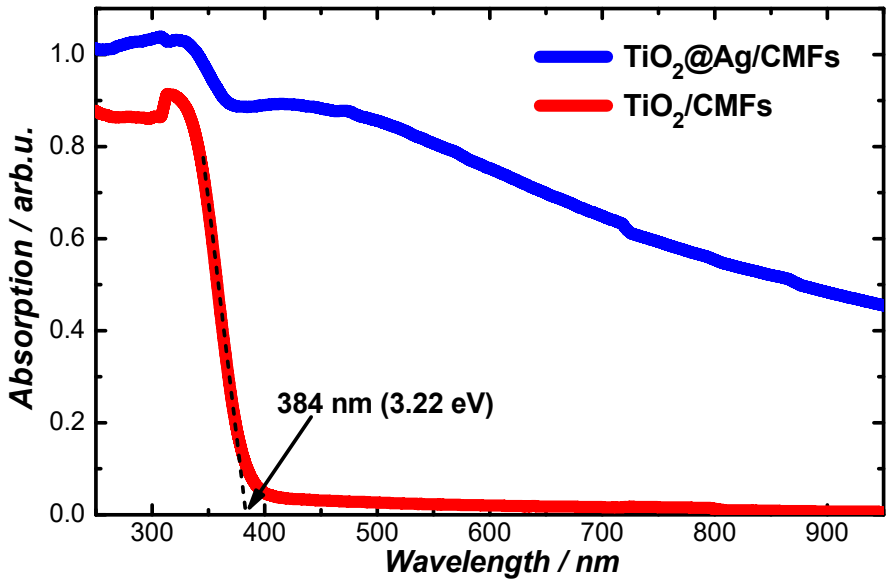

Figure S5. UV-Vis diffuse reflectance spectra of TiO_2/CMFs and TiO_2@Ag/CMFs.

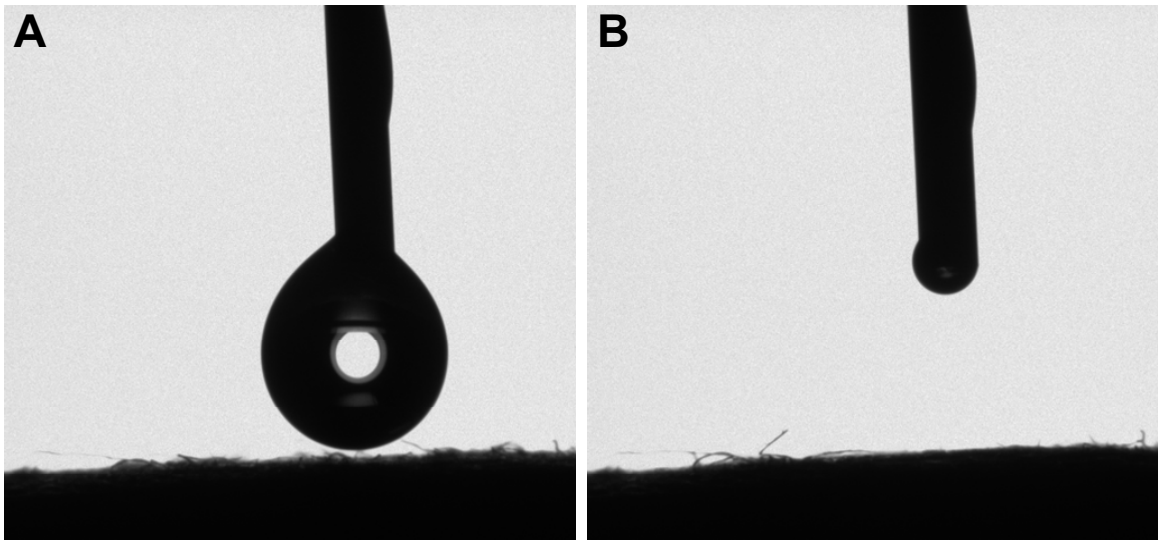

Figure S6. Photographs showing the contact angle toward distilled water on the surfaces of TiO_2@Ag/CMFs: (A) before and (B) immediately after casting a water droplet.

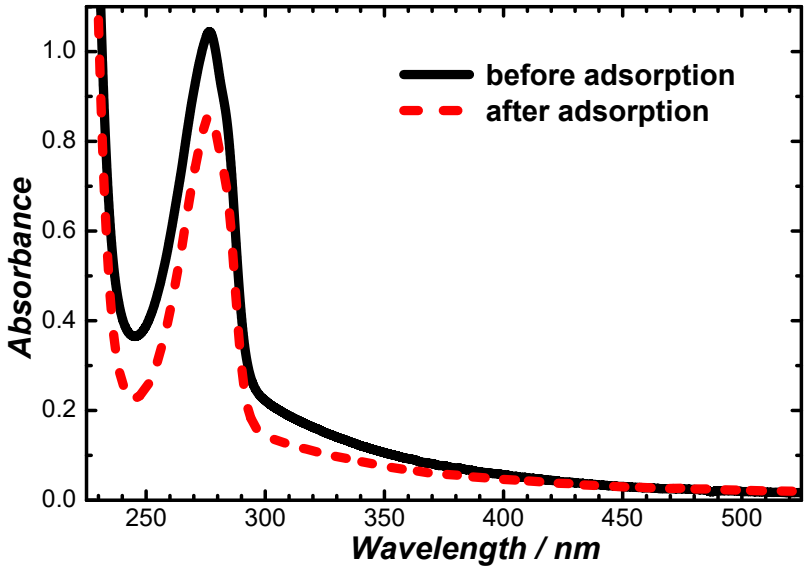

Figure S7. UV-Vis absorption spectra of (A) 4-CP solution (50 mgL^{-1}) and (B) after reaching saturated adsorption upon incubation of 4-CP (200 mL, 50 mg L^{-1}) with 100 mg of TiO_2@Ag/CMFs for 2 h.

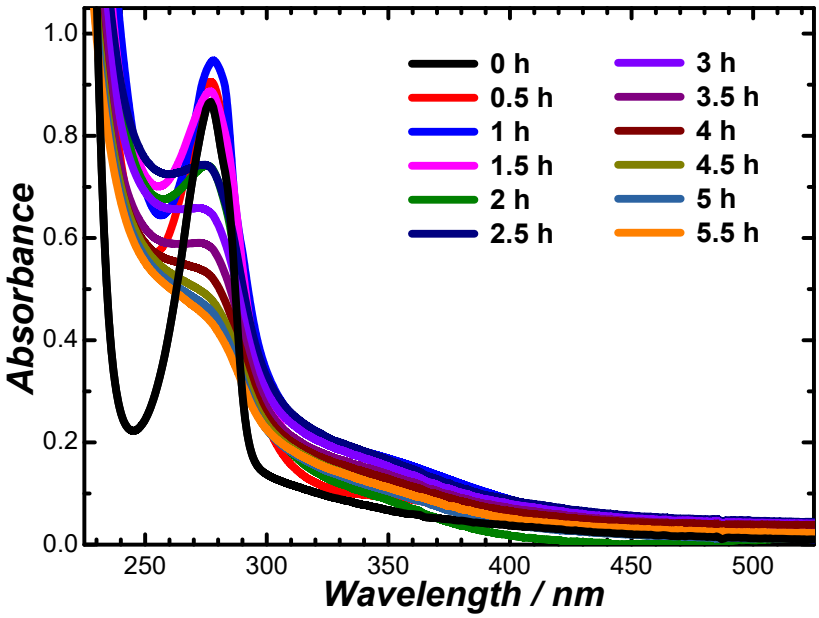

Figure S8. Temporal evolution of UV-Vis absorption spectra of the reaction mixtures during the photocatalytic degradation of 4-CP on TiO_2/CMFs.

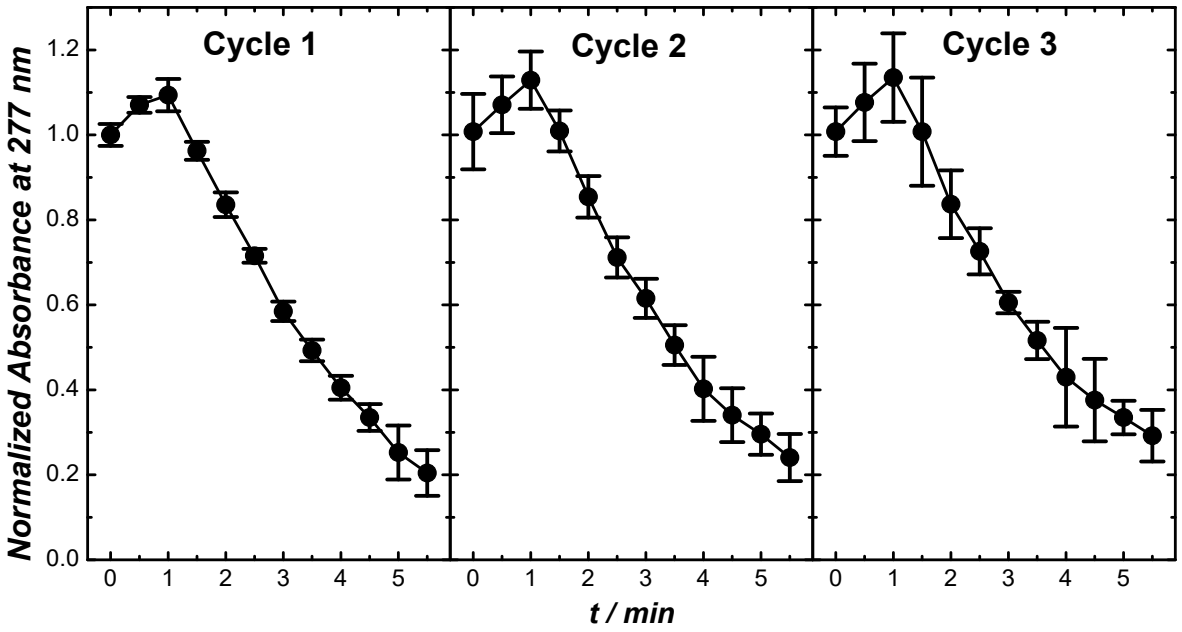

Figure S9. Temporal evolution of absorbance (normalized against the average value of initial absorbance before the reactions started) at λ = 277 nm over three reaction cycles of photocatalytic degradation of 4-CP on TiO_2@Ag/CMFs. The error bars represent the standard deviations obtained from 3 experimental runs.

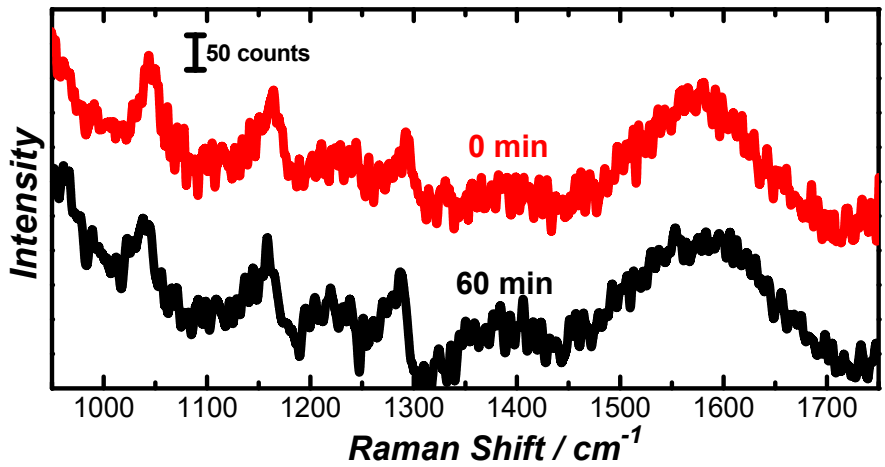

Figure S10. SERS of 4-CP on TiO_2@Ag/CMFs after exposure to a 532 nm confocal laser beam illumination (power: 1 mW; focal area size: 2 μm in diameter) for 0 and 60 minutes. The spectra were offset for clarity.

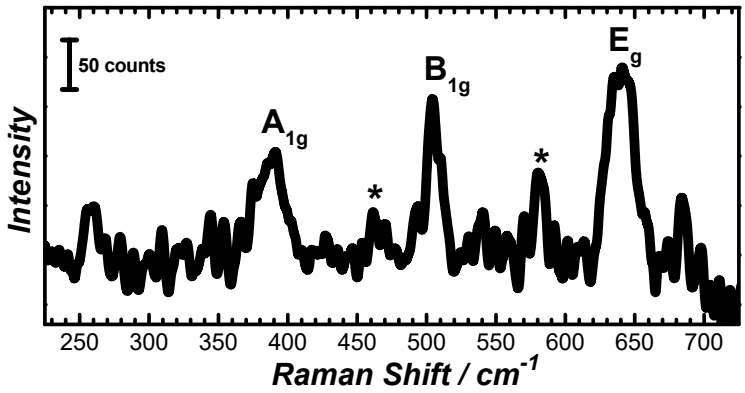

Figure S11. SERS spectra of 4-CP on surfaces of TiO_2@Ag/CMFs in the low wavenumber spectral range from 225 to 725 cm^{-1}. The SERS peaks at 638 cm^{-1}, 505 cm^{-1} and 391 cm^{-1} were assigned to the E_g, B_{1g} and A_{1g} vibrational mode of anatase phase of TiO_2. The Raman peaks labeled with * are characteristic peaks of CMFs.

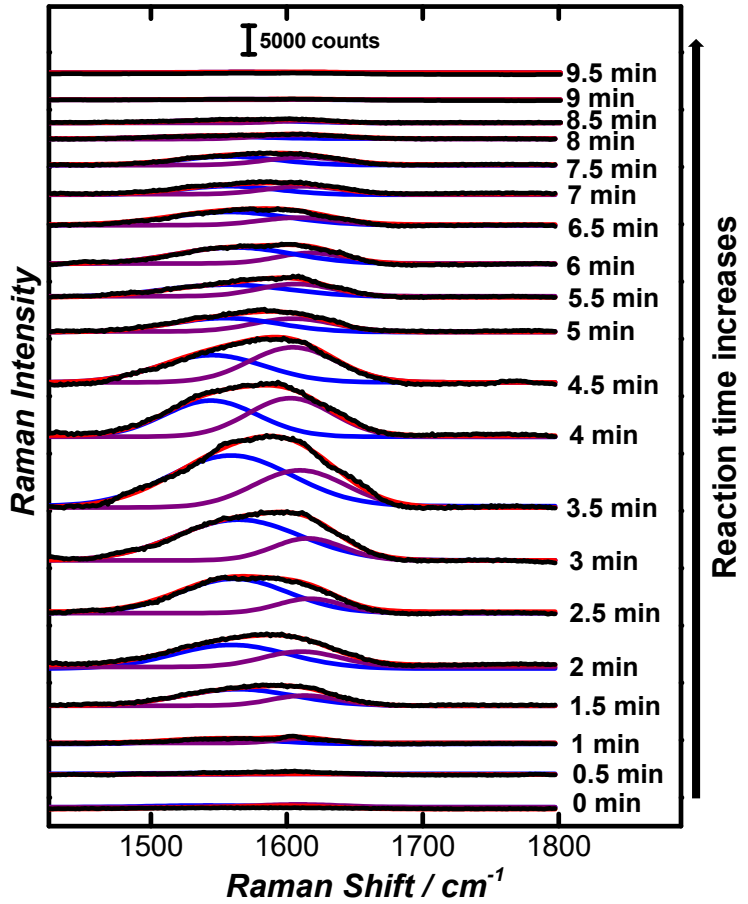

Figure S12. Deconvolution of the SERS peaks at 1605 and 1575 cm^{-1} for time-resolved SERS spectra collected during the photocatalytic degradation of 4-CP on TiO_2@Ag/CMFs.

Table S1. Table listing the assignments of the major Raman peaks.

Raman peak assignment	Peak position in normal Raman spectra	Peak position in SERS spectra
C=O stretching coupled with benzene ring	1657 cm^{-1}	1605 cm^{-1}
C=C stretching in benzene ring	1619 cm^{-1} (4-CP); 1621 cm^{-1} (HQ); 1610 cm^{-1} (BQ)	1575 cm^{-1}
O-H in plane bending	very weak	1390 cm^{-1} (4-CP); 1356 cm^{-1} (HQ, BQ)
C-O stretching of C-OH	1256 cm^{-1}	1295 cm^{-1} (4-CP); 1250 cm^{-1} (HQ, BQ)
C-H in plane bending	1078 cm^{-1} (4-CP); 1163 cm^{-1} (HQ); 1055 cm^{-1} (BQ)	1163 cm^{-1}
C-Cl stretching coupled with benzene ring	1041 cm^{-1}	1048 cm^{-1}